


Escalated Deep-Subwavelength Acoustic Imaging with Field Enhancement Inside a Metalens

Jian Chen^{1,2,†}, Zeqing Sun^{2,†}, Jing Rao³, Danylo Lisevych², and Zheng Fan^{2,*}

¹*The State Key Laboratory of Fluid Power and Mechatronic Systems, School of Mechanical Engineering, Zhejiang University, Hangzhou, 310027, China*

²*School of Mechanical and Aerospace Engineering, Nanyang Technological University, 50 Nanyang Avenue, Singapore 639798, Singapore*

³*School of Engineering and IT, University of New South Wales, Northcott Dr, Campbell ACT 2612, Canberra, Australia*

 (Received 22 June 2021; revised 12 August 2021; accepted 22 September 2021; published 13 October 2021)

Super-resolution acoustic imaging with state-of-the-art spatial resolution ($\lambda/50$), with λ being the wavelength, is showcased with a holey-structured metalens. However, the imaging mechanism under unity transmission based on Fabry-Perot resonances means the metalens fundamentally suffers from narrow bandwidth and limited deep-subwavelength contrast, and therefore further advancement of deep-subwavelength imaging has been stalled. Here we break the barriers for deep-subwavelength acoustic imaging comprehensively in spatial resolution, resolving contrast, and working bandwidth, by exploiting field enhancement inside the metalens. A microscopic model is established to theoretically reveal the underlying physics for escalated deep-subwavelength acoustic imaging. For a proof-of-concept, the imaging performance of the proposed method is numerically proven and experimentally demonstrated. Specifically, a breakthrough resolution below $\lambda/100$ is achieved while resolving contrast is improved by at least 6.5 times and working bandwidth is broadened to approximately 25% of the operating frequency. Furthermore, pulsed acoustic imaging on the deep-subwavelength scale is showcased, which is an important step towards the practical application of the ultrahigh-resolution acoustic imaging technique. We believe the work presented here may greatly benefit a variety of fields in acoustics, such as visualizing subcutaneous structures in medical diagnosis and characterizing subsurface flaws in industrial nondestructive evaluation.

DOI: [10.1103/PhysRevApplied.16.044021](https://doi.org/10.1103/PhysRevApplied.16.044021)

I. INTRODUCTION

Acoustic imaging exerts a profound impact in many fields, such as biomedical diagnosis, nondestructive evaluation (NDE) and structural health monitoring (SHM) [1]. Conventionally, the spatial resolution of an acoustic imaging system is limited by diffraction. This constraint is mainly attributed to far-field effects, where the evanescent waves carrying subwavelength details of imaged objects exponentially vanish. To address this limitation, particularly for deep-subwavelength acoustic imaging, evanescent waves should be available and restored in image formation [2–4].

The past decades have seen exciting theoretical and experimental manipulations of evanescent waves to achieve subwavelength imaging. Amongst these attempts, a superlens with negative effective properties was first proposed [5–9], and thereby motivated the development of

acoustic superlenses composed of acoustic metamaterials (AMMs). Subwavelength imaging has been successfully demonstrated with acoustic superlenses that exhibit negative density [10,11], negative bulk modulus [12,13], or both negative [14] by carefully engineering the AMM microstructures. However, the losses induced by resonance and viscosity noticeably hinder the imaging performance of acoustic superlenses on the deep-subwavelength scale.

Meanwhile, evanescent waves can also be recovered with an AMM lens (acoustic metalens) that supports extreme wave vectors [15–21]. As an example, Fabry-Perot (FP) resonances could produce flat dispersions over a wide range of wave vectors, and thus they can take very large wave-vector values. On this basis, a holey-structured metalens was designed to efficiently excite FP resonances for unity transmission and a state-of-the-art resolution of $\lambda/50$ (λ is the wavelength) was showcased [18]. Nevertheless, this method faces two fundamental constraints, namely, narrow bandwidth and poor deep-subwavelength contrast (as is shown in the following). It is also worth noting that deep-subwavelength acoustic imaging could also

*zfan@ntu.edu.sg

†Jian Chen and Zeqing Sun contributed equally to this work.

be enabled by exciting trapped resonances inside waveguides [22,23]. However, these face similar challenges as the resonant metalens.

To this end, anisotropic AMMs were devised for acoustic hyperlenses, which not only support a wide range of wave vectors but also allow evanescent-to-propagating conversion inside the metamaterial for broadband operation [24–28]. Such behavior was experimentally verified with a fin-shaped hyperlens, which produced subwavelength images over a broad range of frequencies from 4.2 to 7 kHz, rendering a spatial resolution between $\lambda/6.8$ and $\lambda/4.1$ [26]. However, this kind of hyperlens had difficulty performing acoustic imaging on the deep-subwavelength scale. Furthermore, it required the imaged objects to be placed along the inner circumference, which made practical application impossible. Apart from these AMM devices, other strategies, such as the time-reversal technique [29] and image processing algorithms [30], have also been applied for deep-subwavelength acoustic imaging. Nonetheless, the complex setup of the time-reversal approach reduces its robustness and flexibility, while the algorithms add time and complexity to the imaging process.

Inspired by these difficult challenges, it is of great importance to break the barriers in deep-subwavelength acoustic imaging comprehensively regarding spatial resolution, resolving contrast, and working bandwidth. It is worth noting that evanescent wave amplification has been demonstrated inside the holey metalens [17,20]. However, it has mainly been used for subwavelength imaging of subsurface objects at a considerable depth with a highest resolution of $\lambda/25$. On the other hand, the amplification effect has been macroscopically studied

by the effective medium theory, which is not ideal to investigate bandwidth in cases in which surface waves and the coupling effect cannot be ignored. For this reason, whilst broadband characterization is a crucial step towards practical applications, it was left unexplored. In this paper, we report escalated deep-subwavelength acoustic imaging by exploiting field enhancement inside the metalens (Fig. 1). An analytical microscopic model is formulated to theoretically analyze the wave-structure interaction between the point-like evanescent waves and deep-subwavelength waveguides, showing that the pressure field can be enhanced inside the metalens over broadband. Based on this mechanism, the performance of acoustic imaging on the deep-subwavelength scale can be effectively escalated, outperforming the best of what has been available until now in the acoustic regime. For proof-of-concept demonstrations, broadband deep-subwavelength acoustic imaging is numerically and experimentally demonstrated on both one-dimensional (1D) and two-dimensional (2D) defective objects. This study also presents deep-subwavelength imaging with a pulsed source, an important step towards the practical application of deep-subwavelength acoustic imaging in the broad field of acoustics, such as visualizing subcutaneous structures in medical diagnosis and characterizing subsurface flaws in industrial nondestructive evaluation.

II. THEORY AND METHOD

A. Pressure field enhancement inside the metalens

The metalens basically consists of a rigid block of thickness h that is periodically perforated with arrays of deep-subwavelength waveguides (holes) with a lattice constant s . Through FP resonances, all evanescent information on the input surface of the metalens can be conveyed in its entirety to the output surface, and the imaging resolution is geometrically limited by s . This notion may be true under certain circumstances; however, the ultimate resolution is fundamentally restricted by the detectable evanescent waves when the lattice constant is further reduced. To confirm this hypothesis, we numerically investigate the achievable resolution under the mechanism of unity transmission. For clarity, a double slit with a slit width of $\lambda/100$ is used as the imaged object, and the lattice constant of the metalens is set to $\lambda/200$. For ease of comparison, we place the imaging plane 0.01λ away from the metalens, as was done in a previous study [18]. Figure 2(a) shows the pressure field distributions along the x direction as the linewidth (edge-to-edge distance) between the two slits is varied. From the figure, it can be seen that the slits cannot be resolved when the linewidth is below $\lambda/100$, while they can be effectively separated with a linewidth of $\lambda/50$. For comparison, Fig. 2(b) shows the pressure field distribution at the middle plane of the metalens ($z = h/2$). Interestingly, the unresolved slits under unity transmission can be

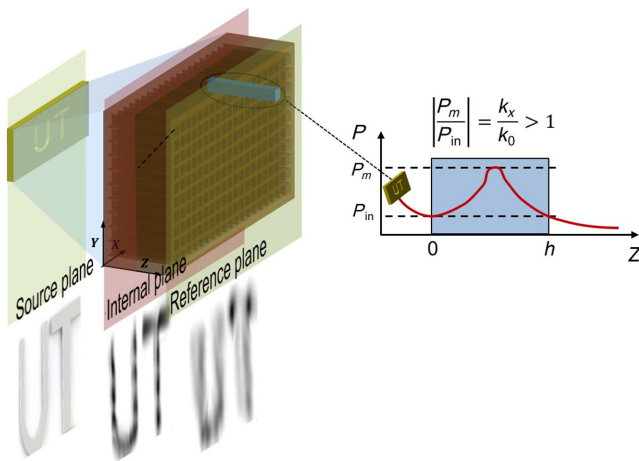


FIG. 1. Illustration of escalated deep-subwavelength acoustic imaging. The schematic metalens consists of an array of deep-subwavelength waveguides perforated in a rigid block with a thickness of h . The inset schematically illustrates the field enhancement inside the deep-subwavelength waveguide. k_x is the tangential wave vector of the evanescent waves.

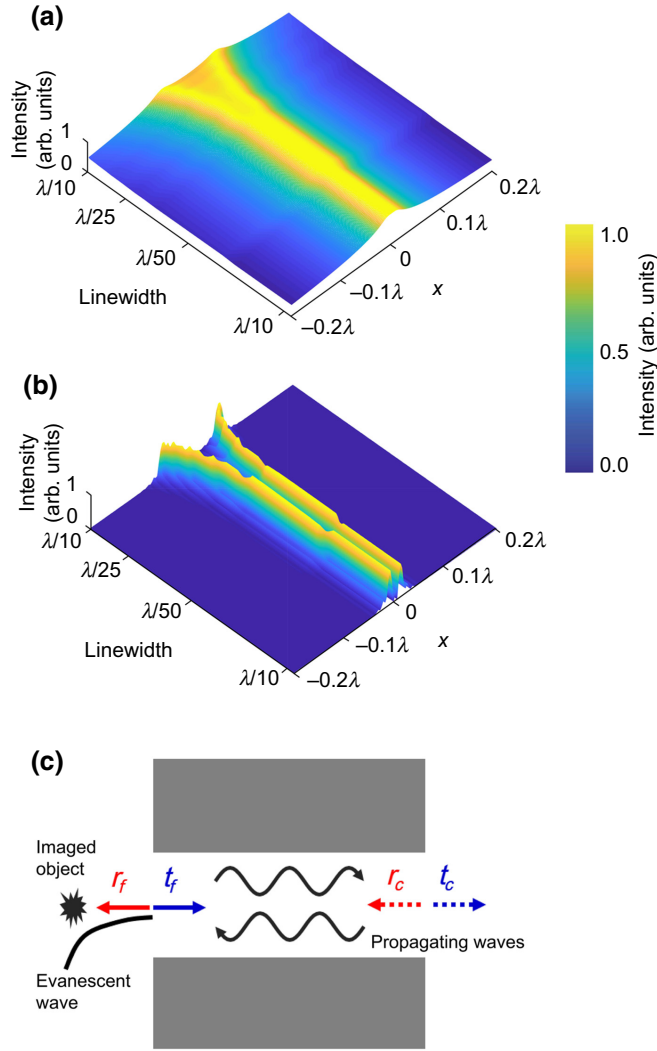


FIG. 2. Pressure field enhancement inside the metalens. (a) and (b) The intensity distributions of the simulated pressure field along the x direction by varying the edge-to-edge distance between two slits in a thin film. The slit width of the source object and the lattice constant of the metalens in the simulation are $\lambda/100$ and $\lambda/200$, respectively. The image planes are located (a) 0.01λ away from the output surface and (b) at the middle plane of the metalens. (c) The fundamental transmission and reflection coefficients between a deep-subwavelength cavity and free space. The evanescent wave is coupled and mode converted into propagating waves inside the waveguide.

clearly distinguished at the middle plane, which provides heuristic evidence that the pressure field of the evanescent waves may be effectively enhanced inside the metalens. For convenience, we refer to deep-subwavelength imaging with unity transmission as the conventional method in the following.

It is worth noting that, under uniform plane-wave incidence, the interaction between the acoustic wave and structures could be macroscopically explained by using effective medium theory (EMT), which approximates the

metalens as a homogeneous medium. Nevertheless, it is difficult to deal with the evanescent waves that are point-like sources. Furthermore, EMT cannot characterize the working bandwidth as the coupling between waveguides cannot be ignored once the resonant condition is not satisfied (as shown in the following). To address these challenges, we develop a microscopic model to reveal the underlying mechanism for escalated deep-subwavelength acoustic imaging, derived from the coupled-mode theory and multiple-scattering formalism [31,32]. To do this, we begin with the fundamental process in a deep-subwavelength cavity, as shown in Fig. 2(c). Within the metamaterial limit ($s \ll \lambda$), the wave-structure interaction is dominated by the wave behavior inside the deep-subwavelength cavity. As a result, the coupling between cavity and free space can be calculated using the coupled-mode theory. For convenience, the transmission and reflection coefficients from free space to the cavity are defined as t_f and r_f , and those from the cavity to free space are denoted as t_c and r_c , respectively. Consider an evanescent wave normally impinging on the cavity aperture, that is ($k_x > k_0$) with k_x and k_0 are tangential wave vector of evanescent waves and acoustic wave number in free space, respectively. In acoustics, the coupled waves can freely propagate inside the cavity because of the absence of a cut-off frequency. In contrast, in the long-wavelength regime, the acoustic field inside the cavity can be well described by the fundamental waveguide mode [33,34]. Combining these notions with boundary conditions, the coefficients can be derived as $t_f = 2/(Y+1)$, $r_f = (1-Y)/(Y+1)$, $t_c = 2Y/(Y+1)$, and $r_c = (Y-1)/(Y+1)$, where $Y = k_0/\sqrt{k_0^2 - k_x^2}$ (see Sec. 1 in Supplemental Material [40]).

Based on these results, the acoustic response of a deep-subwavelength waveguide can be readily described by using multiple-scattering formalism. For example, the transmission and reflection coefficients of the waveguides can be calculated as

$$T(k_x) = \frac{t_f t_c e^{ik_0 h}}{1 - r_c^2 e^{2ik_0 h}} = \frac{4Y e^{ik_0 h}}{(1+Y)^2 - (1-Y)^2 e^{2ik_0 h}} \quad (1)$$

$$R(k_x) = r_f + \frac{t_f r_c t_c e^{2ik_0 h}}{1 - r_c^2 e^{2ik_0 h}} = \left(1 - \frac{4Y e^{2ik_0 h}}{(1+Y)^2 - (1-Y)^2 e^{2ik_0 h}}\right) \left(\frac{1-Y}{1+Y}\right). \quad (2)$$

As expected, unity transmission ($|T(k_x)| = 1$) can be obtained as long as the metalens thickness satisfies $k_0 h = m\pi$ with m being an integer. Under this condition, the reflection is totally suppressed [$R(k_x) = 0$]. In this case, there is no surface wave and the wave dynamics inside the deep-subwavelength waveguide can well represent the metalens. Notably, these findings have been largely

investigated for deep-subwavelength acoustic imaging. Here, as inspired by the interesting phenomena from the numerical investigations, we explore a new imaging method by perceiving the pressure field inside the deep-subwavelength waveguides. To do this, we firstly calculate the pressure field inside the deep-subwavelength waveguide, which can be expressed as

$$P(k_x, z) = \frac{t_f (e^{ik_0 z} + r_c e^{ik_0(2h-z)})}{1 - r_c^2 e^{2ik_0 h}} = \frac{k_x}{k_0} \sin(k_0 z + \phi), \quad (3)$$

where $\phi = \tan^{-1} \left(\sqrt{(k_x/k_0)^2 - 1} \right)$. From Eq. (3), it can be seen intuitively that the pressure field of an evanescent wave [$(k_x/k_0) > 1$] can be effectively enhanced inside the waveguide, which well explains the improvement of spatial resolution at the middle plane as observed. Specifically, the field enhancement linearly scales with k_x , which presents considerable benefits for deep-subwavelength imaging since a fine feature implies a great impact. For example, a fine feature would excite evanescent waves of large k_x and therefore yield great enhancement. As a result, it is highly expected that this mechanism would enable an exciting imaging modality outperforming the conventional method. This is because, under the same detection limit, the very weak evanescent waves overwhelmed by noise in the conventional method may become detectable with the field enhancement. Therefore, escalated deep-subwavelength acoustic imaging becomes possible.

B. Numerical simulation and experimental setup

In this paper, numerical simulations are conducted by using commercial finite-element software COMSOL Multiphysics 5.3a. The simulation model incorporates two

physical modules, which are *Pressure Acoustics* and *Solid Mechanics*. The Multiphysics interface *Acoustic-Structure Boundary* deals with the coupling between them. The host material of the metalens is assigned to be aluminum (Young’s Modulus $E = 70$ GPa, density $\rho = 2700$ kg/m³, and Poisson’s Ratio $\nu = 0.33$), and the filling (background) medium is set to be air (density $\rho = 1.2$ kg/m³ and acoustic velocity $v_1 = 343$ m/s). In the numerical models, the *narrow region acoustic* property is assigned to the deep-subwavelength waveguides to account for the effect of thermal and viscous losses. The imaged objects (samples) are made from thin acrylic plates (Young’s Modulus $E = 3.2$ GPa, density $\rho = 1190$ kg/m³, and Poisson’s Ratio $\nu = 0.35$) that are perforated with a given pattern. To simulate plane-wave incidence, a plane-wave radiation condition is set on the top boundary of the simulation domain. Perfectly matched layers are then imposed on the rest of the boundaries to simultaneously reduce computational burden and prevent spurious reflections. The largest mesh element size is set to be smaller than $\lambda_0/12$, with λ_0 being the shortest incident wavelength. Meanwhile, a refined mesh is applied inside the deep-subwavelength waveguides to account for the fine features at the fluid-solid interfaces. After calculation, the simulated acoustic pressure fields are exported for further analysis and processing in MATLAB 2020.

To validate the theoretical and numerical proofs on deep-subwavelength imaging, an experimental setup is established to perform acoustic field measurements, as schematically shown in Fig. 3. The sample metalens is fabricated through electrical discharge wire cutting (see Fig. S1 in Supplemental Material [40]), and the acoustic field inside the waveguides is measured using laser vibrometry (Polytech GmbH, Germany). For clarity, the basic principle and configuration for optical measurement

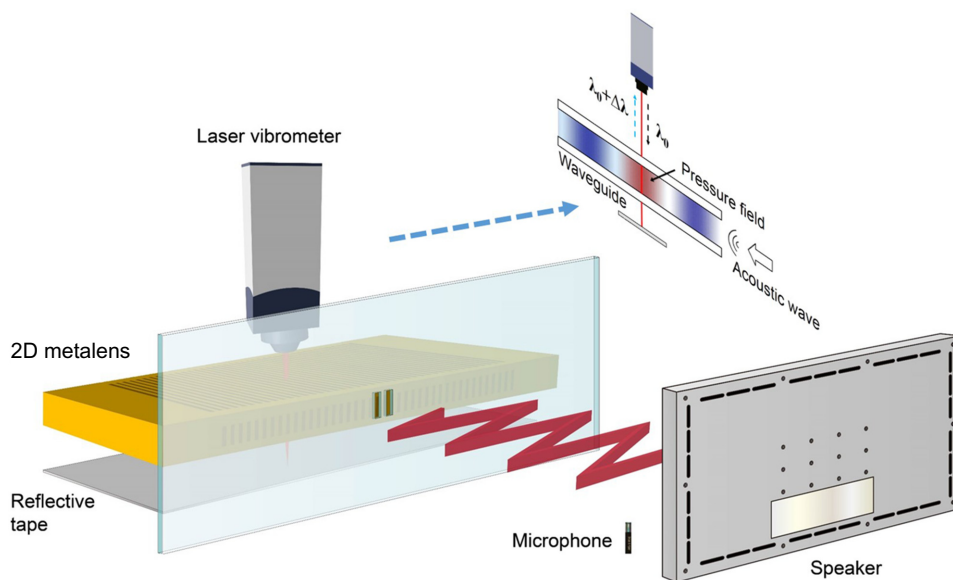


FIG. 3. The schematic of the experimental setup for acoustic field measurements. The inset shows the basic principle and configuration for optical measurement of an acoustic wave inside the deep-subwavelength waveguide.

of acoustic waves inside the waveguide is shown in the inset. A square speaker (Sound Shower, Panphonics, USA), controlled by multifunction virtual instrument software, is used to generate plane-wave incidence. The plane wave impinges on the imaged objects and the scattered waves from the objects are coupled into the waveguides. To map the field distribution inside the metalens, the laser vibrometer, consisting of an OFV-505 optical head and an OFV-5000 controller, is scanned point-by-point with a lab-made scanning stage. Notably, transparent glass with an antireflection coating ($R_{av} \leq 0.5\%$, Edmund Optics, USA) covers the side faces of the metalens to enhance optical transmission, and this also seals the waveguides. To minimize perturbation of the optical measurements of acoustic waves inside the metalens, an acoustic window is applied on the sample that can block the transmitted waves outside the metalens. Meanwhile, a microphone (Type 4961, B&K, Denmark) is placed right before the speaker to record the incident wave, which is used to normalize the experimental measurements and synchronize the acquisition. At each point, the acoustic signals are averaged over 100 times to improve the signal-to-noise ratio. To reduce undesired wave reflections and ambient noise, the experiments are carried out in an anechoic room.

III. RESULTS AND DISCUSSIONS

A. Broadband deep-subwavelength imaging of defective objects

The presence of tiny defects, such as subsurface cracks and inclusions, would greatly affect the integrity of fundamental materials and key structural components, thus may bring serious damage, even disasters, in various fields, such as aerospace engines, nuclear plants, and civil infrastructure. Therefore, as an important member of the NDE and SHM family, acoustic-imaging-based defect evaluation is becoming increasingly important. To this end, we begin with a proof-of-concept study on a defective object to preliminarily corroborate the proposition for escalated deep-subwavelength imaging. At first, results are tested for spatial resolution and resolving contrast. For ease of sample fabrication and experimental measurements, the operating frequency is chosen to be $f = 2580$ Hz ($\lambda = 133$ mm). The geometrical parameters of the metalens are set as $s = 1.5$ mm ($\lambda/89$), $a = 1.0$ mm, and $h = 66.5$ mm. For simplicity but without loss of generality, we consider an imaged object consisting of four tiny defects. The defect widths are 1.5 mm and the linewidths between them are 1.5, 10.5, and 3 mm, respectively, as depicted on the top of Fig. 4(a). To efficiently couple the scattered waves, the source object is placed in contact with the metalens directly.

Figure 4(a) shows the intensity distribution of simulated pressure field inside the metalens. Compared to that on

the output surface ($z = h$), a remarkable enhancement of pressure field can be observed inside the metalens, particularly in the middle region. Moreover, such enhancement only occurs in the waveguides aligning with the defective features, which provides direct proof that the defects can be effectively identified. As a quantitative examination, the amplitude profiles of the simulated pressure fields along the horizontal (x) direction at the middle plane and output surface are both plotted in Fig. 4(c). As a reference, the amplitude profile at the imaging plane that is 0.01λ away from the metalens is likewise plotted. As can be seen, all of the defective features can be accurately imaged at the output surface, which is a perfect replica of the source object under unity transmission. Nevertheless, the two closely spaced features cannot be resolved at the reference plane, indicating that the evanescent waves regarding fine features decay very quickly and are difficult to perceive even in very close proximity to the metalens. However, they can be easily separated inside the metalens. Accordingly, a spatial resolution of $\lambda/89$ is readily obtained with the proposed method. Furthermore, the pressure amplitude inside the metalens also increases by approximately 9 times compared with that on the input and output surfaces. Apart from spatial resolution, the resolving contrast is also substantially improved. For clarity, here the resolving contrast is defined as $C = (P_{\max} - P_{\min})/P_{\max}$, where P_{\max} and P_{\min} denote the pressure amplitude at the peak and valley, respectively (see Fig. S2 for the illustration in Supplemental Material [40]). As can be seen from Fig. 4(c), P_{\max} and P_{\min} at the middle plane (red line) are 4.2 and 0.67 Pa, respectively. As a result, the resolving contrast is calculated to be 0.84. Similarly, the resolving contrast at the source plane (source contrast) is 0.13, with P_{\max} and P_{\min} being 0.53 and 0.46 Pa (blue line). It is worth emphasizing that the source contrast is the best that can be obtained with the conventional method. As a result, we can conclude that, through examination of the pressure field inside the metalens, the resolving contrast of the proposed method can be improved by at least 6.5 times over the conventional method. Meanwhile, Fig. 4(a) shows that the field enhancement remains evident within a considerably enlarged region (white dashed rectangle). Differing from the conventional method, the imaging performance of the proposed method is not sensitive to the probing location and would not change too much as long as the pressure field is perceived within this region. Therefore, the proposed method will be quite robust and beneficial for practical applications. To date, the simulated results prove that the proposed method is effective for escalated deep-subwavelength acoustic imaging in both spatial resolution and resolving contrast.

To experimentally verify the effectiveness of the proposed method, we also measure the pressure field inside the metalens by using a laser vibrometer [35]. Compared with a microphone, the optical method would

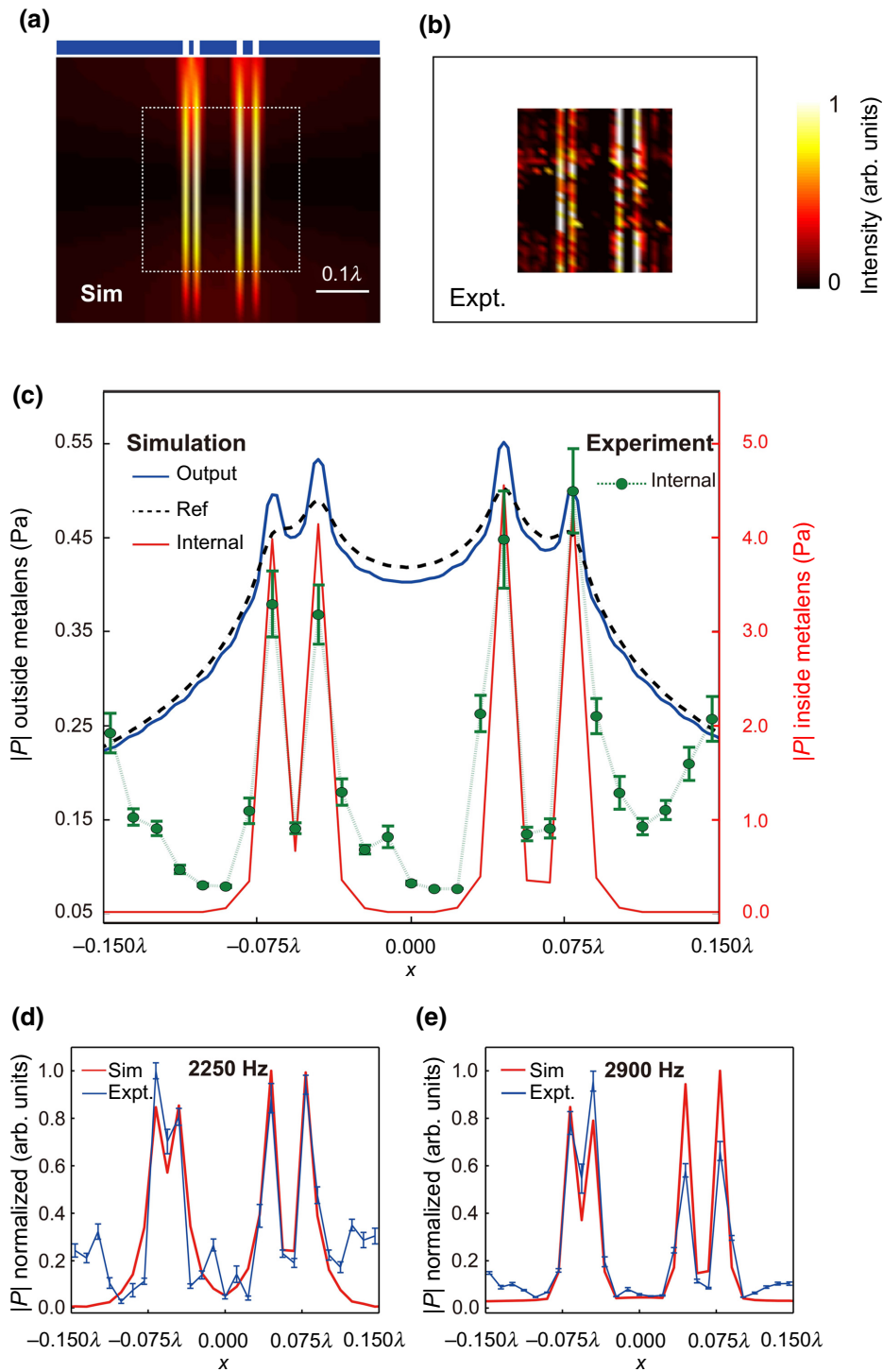


FIG. 4. Broadband deep-subwavelength imaging of defective object. (a) and (b) The normalized intensity maps of (a) simulated and (b) measured pressure fields inside the metalens. The white dashed rectangle in (a) shows the measurement area in the experiments. The inset in (a) above the image schematically shows the imaged object. (c) The pressure amplitude profiles along the horizontal (x) direction at different imaging planes. The solid lines represent the simulated profiles at the output surface (blue), internal plane (red), and reference plane (black), respectively. The reference imaging plane is 0.01λ away from the output surface. The measured profile at the internal plane (green dashed symbol) is averaged by 10 measurements and mapped to the simulated pressure field for ease of comparison. (d) and (e) The normalized amplitude profiles of simulated and measured pressure fields at the internal plane at (d) 2250 Hz and (e) 2900 Hz. The simulated and measured results are normalized to their respective maximum values. The measured results are averaged over 10 measurements.

significantly minimize the perturbation of the pressure field inside the deep-subwavelength waveguide. For comparison, Fig. 4(b) shows the intensity distribution of the measured pressure field [white dashed rectangle in Fig. 4(a)], which exhibits good consistency with the simulated map. Pressure field enhancement is also clearly shown inside the metalens, aligning well with the defective features. For ease of comparison, the measured amplitude profile

along the x direction is also plotted in Fig. 4(c). It can be seen that the experimental and simulated results are in good agreement, once again confirming the feasibility of the proposed method for escalated acoustic imaging on the deep-subwavelength scale. Note that although the sensitivity of optical detection is markedly lower than that of the microphone, the deep-subwavelength features can still be accurately reproduced. In other words,

the imaging performance may be further improved with other acoustic sensors of high sensitivity. Overall, the experimental results also support the hypothesis of escalated deep-subwavelength acoustic imaging.

Now that the enhancement of deep-subwavelength imaging on spatial resolution and resolving contrast is confirmed, we likewise examine the bandwidth. It is well known that the working bandwidth of the conventional method is greatly limited. This is because the deep-subwavelength details rapidly blur even if the resonant condition is just slightly detuned. In this sense, we anticipate a broadband performance if the field enhancement inside the deep-subwavelength waveguides can be preserved when the resonant condition is considerably detuned. To show this, we investigate field enhancement with resonance detuning using the microscopic coupled-wave model [36]. Note that the incident evanescent wave is considered to be a point source that is distributed on the deep-subwavelength aperture, and the pressure amplitude is then calculated in the middle of the waveguide. From the calculations, it can be seen that the amplification effect ($|P/P_{in}| > 3$) remains effective for the evanescent waves when the resonance condition is considerably detuned (see Fig. S3 in Supplemental Material [40]). As a result, it would be highly possible to reproduce the deep-subwavelength details over broadband. To further confirm this assertion, we numerically examine the pressure field distributions at different frequencies while keeping the metalens structure unchanged (see Fig. S4 in Supplemental Material [40]). As expected, the field enhancement is effectively preserved over a broad frequency range, and therefore deep-subwavelength imaging over broadband may be readily foreseen. To render direct proof, the source object is numerically and experimentally imaged at 2250 Hz [Fig. 4(d)] and 2900 Hz [Fig. 4(e)]. Note that the lower and upper limits of the operation band (2250 and 2900 Hz) are determined by numerical simulations, at which the resolving contrast is still larger than the best of what is possible with the conventional method, i.e., the source contrast. It can be seen that the simulated and measured results are in good agreement, and the linewidth of 1.5 mm ($\lambda/104$ – $\lambda/79$) can be clearly resolved at both frequencies. Thus, we also demonstrate escalated deep-subwavelength acoustic imaging on a working bandwidth that is approximately 25% of the operating frequency, which is substantially larger than most resonance-based imaging systems.

B. Deep-subwavelength imaging of complex objects with a pulse wave

In practical applications of acoustic imaging, a pulse wave is the most widely used source. Compared to the continuous counterpart, backscattered pulse waves could provide much more information, such as

time-of-flight for object localization, wave dynamics in propagation, and dispersive effects on wave-structure interaction. For this reason, acoustic imaging with a pulse wave is a critical step towards practical applications. On the other hand, compared with the 1D case, a 2D complex object is more common in reality; however, it is also much more challenging owing to complex features and details.

To this end, we showcase deep-subwavelength acoustic imaging of complex 2D objects with pulsed plane-wave incidence. As a concrete example, the logo of Nanyang Technological University (“NTU”) made from a thin acrylic plate is used as the imaged object, as shown in Fig. 5(a). The width and height of the perforated letters are 19.5 and 30 mm, respectively, and the separation between them is 3 mm. Similar to the setup described previously, the object is placed directly in front of the metalens. To accommodate the working bandwidth, a Gaussian-windowed pulse wave with a central frequency of 2580 Hz and a -6 dB bandwidth of 650 Hz is excited by the speaker. Note that the experimental setup cannot acquire the whole image of the 2D object with one projection. Instead, each waveguide functions as a sampling pixel in the imaging process, and the image is formed by performing pixel-to-pixel scanning. For clarity, the imaging process is schematically illustrated in Fig. 5(b). To acquire the data for all pixels, the imaging process consists of two scanning procedures (see Supplemental Material Movie S0 [40]). Firstly, the laser vibrometer scans to record the acoustic field inside each metalens cavity with a step size that is same as the lattice constant, as denoted by the orange arrow in Fig. 5(b). After that, the metalens is moved to new imaging position (blue arrow), and then the laser vibrometer scans again. These two procedures are alternately repeated until all pixels are sampled, and the full image is finally obtained.

As a representation, Fig. 5(c) shows the time traces of pulse waves scattered from the imaged object [white dashed line in Fig. 5(a)], from which the evolution of the scattered waves can be obtained. It can be seen that the complex object is well imaged in the time domain and remains evident during the whole time period (see Supplemental Material Movies S1 and S2 [40]). However, this is not the case for the conventional method (see Supplemental Material Movie S3 [40]). Meanwhile, the acoustic images at different frequencies are also obtained with Fourier transformation of the time-trace signals. Figure 5(e) shows the simulated and measured results at 2580 Hz, both of which demonstrate that the perforated letters are accurately reproduced, thereby proving the proposed method can thoroughly image complex objects on the deep-subwavelength scale. However, it is worth noting that the resolving contrast of large features (the perforations along the x direction), such as the upper part of “T” and lower part of “U”, is comparatively low. This is

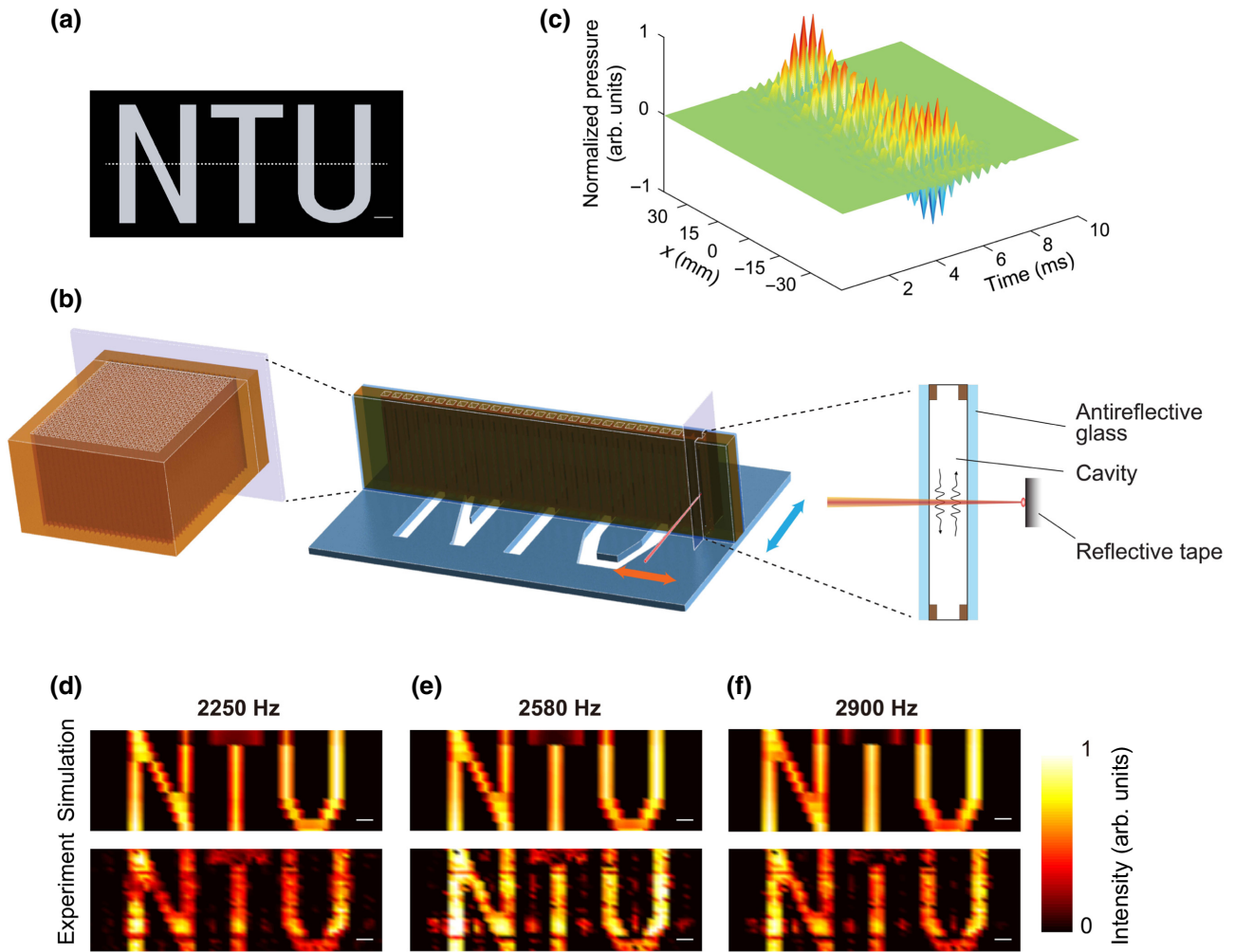


FIG. 5. Deep-subwavelength imaging of complex objects with a pulse wave. (a) The target image of Nanyang Technological University logo. The letters “NTU” are perforated in an acrylic plate. Scale bar, 5 mm. (b) The schematic illustration of the imaging process for pixel-to-pixel sampling. Antireflective glass is used to enhance the optical transmission and seal the waveguides. For better visualization, the objects (metalens, sample, and optical beam) are not to scale. (c) The time traces of the pulse waves along the white dashed line in (a). The pulse waves are recorded at the middle plane of the metalens. (d)–(f) The simulated and measured images at different frequencies: (d) 2250 Hz, (e) 2580 Hz, and (f) 2900 Hz. The simulated and measured pressure fields are obtained at the middle plane of the metalens. The intensity is normalized at the respective frequency. White bars correspond to a length of 5 mm.

reasonable as the field enhancement for these features is relatively low. On the other hand, the edges can excite very high spatial-frequency evanescent waves and yield large enhancement. Nevertheless, as signified in Eq. (3), such field enhancement takes place away from the middle plane, and in turn, the resolving contrast is moderate. Similarly, the acoustic images are also acquired at 2250 Hz [Fig. 5(d)] and 2900 Hz [Fig. 5(f)] to check the broadband performance. Despite mild blurring, the patterns are still intact and can be easily identified. As expected, the resolving contrasts of the large features is further deteriorated when the frequency increases. Overall, these results fully indicate that escalated deep-subwavelength imaging is also effective in complicated scenarios and underpins the great potential of the proposed method for practical applications.

IV. CONCLUSION

In conclusion, we theoretically analyze, numerically prove, and experimentally demonstrate escalated acoustic imaging on the deep-subwavelength scale through field enhancement inside the metalens. Numerical simulations and experimental measurements are conducted on both 1D and 2D defective objects, yielding promising results with good agreement. Therefore, the effectiveness of escalated deep-subwavelength acoustic imaging is readily confirmed. In particular, the proposed method outperforms the conventional method comprehensively in spatial resolution, resolving contrast and working bandwidth. Specifically, a breakthrough of spatial resolution below $\lambda/100$ is realized, and the working bandwidth is

broadened to roughly 25% of the operating frequency. Moreover, deep-subwavelength acoustic imaging of complex objects with a pulse wave is also showcased, therefore underpinning its great potential in practical applications. It is also worth noting that although the achievable resolution is currently restricted by the lattice constant, it may be further advanced by reducing the spacing of deep-subwavelength waveguides. However, it must be pointed out that the actual resolution is compromised by thermal and viscous losses when the waveguide spacing is shrunk. Additionally, the spatial resolution is affected by the sensitivity of acoustic sensors, as well as the gap between the source object and metalens (see Sec. 2 in Supplemental Material [40]).

Beyond the scope of this work, several concerns need to be addressed in the near future. Firstly, the imaging process based on pixel-to-pixel sampling is time-consuming. Ideally, the imaging system is capable of directly projecting the imaged object in real time. Nevertheless, the rapid development of miniaturized acoustic sensors, such as photonic acoustic sensors, cavity optomechanical sensors, and coatable nanocomposite sensors, provides great potential for rapid data acquisition with sensor arrays [37–39]. With great efforts towards the development of integration technologies, real-time imaging can be foreseen by integrating a miniaturized sensor array inside the metalens. Secondly, the proposed method is primarily showcased with plane-wave incidence, and the imaging performance may be further improved with the incidence of a focusing wave [36]. In this case, the acoustic energy could be concentrated within a desired volume and therefore increase the signal-to-noise ratio in acoustic imaging. The metalens can also be scaled to other sizes of interest and other operating frequencies according to the application. We strongly believe the proposed method may find great potential in ultrahigh-resolution imaging for ultrasonic applications together with microelectromechanical systems technology. Finally, the findings presented here may make electromagnetic counterparts intriguing because of the similarities between sound and electromagnetic waves.

ACKNOWLEDGMENTS

This work is supported by the Ministry of Education Singapore under Grant No. MOE2019-T2-2-068 and National Natural Science Foundation of China under Grant No. 52075486.

Z.F. conceived the idea. J.C. carried out theoretical calculations and numerical simulations. Z.S. conducted experiments and data analysis. J.R. and D.L. established experimental setup. Z.F. supervised the work. J.C. wrote the manuscript, and all authors reviewed the manuscript.

The authors declare that they have no conflict of interest.

- [1] W. S. Gan, *Acoustical Imaging: Techniques and Applications for Engineers* (John Wiley & Sons, Hoboken, NJ, USA, 2012).
- [2] J. Park, C. Park, H. S. Yu, J. Park, S. Han, J. Shin, S. H. Ko, K. T. Nam, Y. H. Cho, and Y. K. Park, Subwavelength light focusing using random nanoparticles, *Nat. Photon.* **7**, 454 (2013).
- [3] G. Ma and P. Sheng, Acoustic metamaterials: From local resonances to broad horizons, *Sci. Adv.* **2**, e1501595 (2016).
- [4] H. Ge, M. Yang, C. Ma, M. H. Lu, Y. Chen, N. Fang, and P. Sheng, Breaking the barriers: Advances in acoustic functional materials, *Nat. Sci. Rev.* **5**, 159 (2018).
- [5] J. B. Pendry, Negative Refraction Makes a Perfect Lens, *Phys. Rev. Lett.* **85**, 3966 (2000).
- [6] N. Fang, H. Lee, C. Sun, and X. Zhang, Sub-diffraction-limited optical imaging with a silver superlens, *Science* **308**, 534 (2005).
- [7] T. Taubner, D. Korobkin, Y. Urzhumov, G. Shvets, and R. Hillenbrand, Near-field microscopy through a SiC superlens, *Science* **313**, 1595 (2006).
- [8] I. I. Smolyaninov, Y. J. Hung, and C. C. Davis, Magnifying superlens in the visible frequency range, *Science* **315**, 1699 (2007).
- [9] X. Zhang and Z. W. Liu, Superlenses to overcome the diffraction limit, *Nat. Mater.* **7**, 435 (2008).
- [10] K. Deng, Y. Ding, Z. He, H. Zhao, J. Shi, and Z. Liu, Theoretical study of subwavelength imaging by acoustic metamaterial slabs, *J. Appl. Phys.* **105**, 124909 (2009).
- [11] J. J. Park, C. M. Park, K. J. B. Lee, and S. H. Lee, Acoustic superlens using membrane based metamaterials, *Appl. Phys. Lett.* **106**, 051901 (2015).
- [12] M. Ambati, N. Fang, C. Sun, and X. Zhang, Surface resonant states and superlensing in acoustic metamaterials, *Phys. Rev. B.* **75**, 195447 (2007).
- [13] N. Kaina, F. Lemoult, M. Fink, and G. Lerosey, Negative refractive index and acoustic superlens from multiple scattering in single negative metamaterials, *Nature* **525**, 77 (2015).
- [14] S. Zhang, L. L. Yin, and N. Fang, Focusing Ultrasound With an Acoustic Metamaterial Network, *Phys. Rev. Lett.* **102**, 194301 (2009).
- [15] X. Ao and C. T. Chan, Far-field image magnification for acoustic waves using anisotropic acoustic metamaterials, *Phys. Rev. E* **77**, 025601 (2008).
- [16] J. Christensen and F. J. G. de Abajo, Anisotropic Metamaterials for Full Control of Acoustic Waves, *Phys. Rev. Lett.* **108**, 124301 (2012).
- [17] Y. Cheng, C. Zhou, Q. Wei, D. Wu, and X. Liu, Acoustic subwavelength imaging of subsurface objects with acoustic resonant metalens, *Appl. Phys. Lett.* **103**, 224104 (2013).
- [18] J. Zhu, J. Christensen, J. Jung, L. Martin-Moreno, X. Yin, L. Fok, X. Zhang, and F. J. Garcia-Vidal, A holey-structured metamaterial for acoustic deep-subwavelength imaging, *Nat. Phys.* **7**, 52 (2011).
- [19] K. K. Amireddy, K. Balasubramaniam, P. Rajagopal, Deep subwavelength ultrasonic imaging using optimized holey structured metamaterials, *Sci. Rep.* **7**, 7777 (2017).
- [20] B. Yuan, J. Liu, C. Liu, Y. Cheng, and X. Liu, Resonant tunneling compression and evanescent wave amplification by an acoustic metalens, *Appl. Acoust.* **178**, 107993 (2021).

- [21] S. A. Cummer, J. Christensen, and A. Alu, Controlling sound with acoustic metamaterials, *Nat. Rev. Mater.* **1**, 16001 (2016).
- [22] M. Moleron and C. Daraio, Acoustic metamaterial for sub-wavelength edge detection, *Nat. Commun.* **6**, 8037 (2015).
- [23] C. Ma, S. Kim, and N. Fang, Far-field acoustic subwavelength imaging and edge detection based on spatial filtering and wave vector conversion, *Nat. Commun.* **10**, 204 (2019).
- [24] J. Li, L. Fok, X. B. Yin, G. Bartal, and X. Zhang, Experimental demonstration of an acoustic magnifying hyperlens, *Nat. Mater.* **8**, 931 (2009).
- [25] D. Lu and Z. Liu, Hyperlenses and metalenses for far-field super-resolution imaging, *Nat. Commun.* **3**, 1205 (2012).
- [26] V. M. Garcia-Chocano, J. Christensen, and J. Sanchez-Dehesa, Negative Refraction and Energy Funneling by Hyperbolic Materials: An Experimental Demonstration in Acoustics, *Phys. Rev. Lett.* **112**, 144301 (2014).
- [27] C. Shen, Y. B. Xie, N. Sui, W. Wang, S. A. Cummer, and Y. Jing, Acoustic Planar Hyperlens Based on Anisotropic Density-Near-Zero Metamaterials, *Phys. Rev. Lett.* **115**, 254301 (2015).
- [28] G. Song, W. Jiang, Q. Cheng, L. Wu, H. Dong, and T. J. Cui, Acoustic magnifying lens for far-field high resolution imaging based on transformation acoustics, *Adv. Mater. Technol.* **2**, 1700089 (2017).
- [29] G. Lerosey, J. de Rosny, A. Tourin, and M. Fink, Focusing beyond the diffraction limit with far-field time reversal, *Science* **315**, 1120 (2007).
- [30] P. Arbelaez, M. Maire, C. Fowlkes, and J. Malik, Contour detection and hierarchical image segmentation, *IEEE Trans. Pattern Anal.* **33**, 898 (2011).
- [31] M. Lu, X. Liu, L. Feng, J. Li, C. Huang, Y. Chen, Y. Zhu, S. Zhu, and N. Ming, Extraordinary Acoustic Transmission Through a 1D Grating with Very Narrow Apertures, *Phys. Rev. Lett.* **99**, 174301 (2007).
- [32] Y. Zhou, M. Lu, L. Feng, X. Ni, Y. Chen, Y. Zhu, S. Zhu, and N. Ming, Acoustic Surface Evanescent Wave and its Dominant Contribution to Extraordinary Acoustic Transmission and Collimation of Sound, *Phys. Rev. Lett.* **104**, 164301 (2010).
- [33] Y. Takakura, Optical resonance in a narrow slit in a thick metallic screen, *Phys Rev Lett.* **86**, 5601 (2001).
- [34] R. Al Jahdali and Y. Wu, High transmission acoustic focusing by impedance matched acoustic meta-surfaces, *Appl. Phys. Lett.* **108**, 031902 (2016).
- [35] R. Malkin, T. Todd, and D. Robert, A simple method for quantitative imaging of 2D acoustic fields using refractovibrometry, *J. Sound Vib.* **333**, 4473 (2014).
- [36] J. Chen, J. Xiao, D. Lisevych, A. Shakouri, and Z. Fan, Deep-subwavelength control of acoustic waves in an ultracompact metasurface lens, *Nat. Commun.* **9**, 4920 (2018).
- [37] G. Wissmeyer, M. Pleitez, A. Rosenthal, and V. Ntziachristos, Looking at sound: Optoacoustics with all-optical ultrasound detection, *Light Sci. Appl.* **7**, 53 (2018).
- [38] S. Basiri-Esfahani, A. Armin, S. Forstner, and W. Bowen, Precision ultrasound sensing on a chip, *Nat. Commun.* **10**, 132 (2019).
- [39] Z. Zeng, M. Liu, H. Xu, W. Liu, Y. Liao, H. Jin, L. Zhou, Z. Zhang, and Z. Su, A coatable, light-weight, fast-response nanocomposite sensor for the in situ acquisition of dynamic elastic disturbance: From structural vibration to ultrasonic waves, *Smart Mater. Struct.* **25**, 065005 (2016).
- [40] See Supplementary Videos at <http://link.aps.org/supplemental/10.1103/PhysRevApplied.16.044021> for the imaging processes and deep-subwavelength imaging in time domain.